Brodogradnja Volume 76 Number 4 (2025) 76407

journal homepage: www.brodogradnja.fsb.hr

Brodogradnja

An International Journal of Naval Architecture and Ocean Engineering for Research and Development

Structural Strength Evaluation of a Planing Hull Based on a One-way Coupled CFD-FEA

Jianjun Tu[12], *Feng Feng*[1], *Yang Lu*[*1], *Shiwei Wang*[2], *Qian Cao*[2]

1 College of Shipbuilding Engineering, Harbin Engineering University, Harbin, 150001, China
2 Heilongjiang Water Transport Planning and Design Institute Co., Ltd., Harbin 150001, China

ARTICLE INFO

Keywords:
Planing hull
Computational fluid dynamics
Finite-element analysis
Wave load
Structural strength

ABSTRACT

This study employs a one-way coupling method based on CFD and FEA to evaluate and compare the structural strength of a planing hull under calm water and wave navigation conditions. A high-speed planing hull is selected as the research object. The wave loads under different navigation states are computed using the CFD method, and the pressure distribution on the hull bottom is mapped to a finite element model for structural strength analysis. The study investigates the variations in hull bottom pressure and structural stress under three navigation states: displacement, semi-planing, and planing. Additionally, the stress characteristics under wave conditions, including hogging and sagging states, are simulated and evaluated. By comparing the results with those obtained from the conventional empirical formula method, the accuracy and advantages of CFD in wave load calculations are validated, and the localized stress concentration areas under calm planing conditions are identified. The results demonstrate that this method not only enhances the precision of wave load calculations but also provides an effective approach for structural strength evaluation in planing hull design, thereby improving the technical and economic performance of planing hulls.

1. Introduction

Researching hull strength and conducting reasonable structural design are critical to ensuring the safety of hull structures. Accurately determining the design value of wave loads is key to evaluating the rationality and safety of structural designs [1, 2]. For standard hull types, classification societies have derived empirical formulas to predict wave loads based on extensive model and full-scale ship tests [3]. However, for non-standard hull types, wave load design values are typically obtained through model tests or hydrodynamic software-based direct calculations [4].

Before 1955, wave load calculations mainly relied on Timoshenko wave theory for strength evaluation [5]. With the advent of ship strip theory and advancements in hydrodynamic software, the accuracy of wave load calculations has significantly improved [6]. Compared to empirical formulas, hydrodynamic software can more accurately account for hull geometry and sailing posture, making it suitable for wave load

* Corresponding author.
E-mail address: luyang@hrbeu.edu.cn

https://doi.org/10.21278/brod76407
Received 2 April 2025; Received in revised form 4 July 2025; Accepted 28 July 2025
Available online 7 August 2025
ISSN 0007-215X; eISSN 1845-5859

calculations across various ship types. In contrast to model tests, hydrodynamic software avoids scale effects, reduces time and cost, and can simulate more complex operating conditions [7, 8], particularly excelling in modeling nonlinear phenomena such as wave breaking and impact [9].

The navigation state of a planing hull varies with speed, and the volumetric Froude number is commonly used to characterize its state [10]. Unlike conventional ships, the flotation attitude and wave impact load distribution on the bottom of a planing hull change with speed, making the pressure distribution on the hull bottom critical for strength evaluation. Several studies have investigated the wave impact problem of planing hulls [11-14]. In the preliminary design stage of planing hulls, accurately calculating wave loads and evaluating structural strength are essential for optimizing design and improving operational efficiency.

Depending on computational demands and fidelity requirements, researchers have developed both one-way and two-way coupled FSI (Fluid-Structure Interaction) strategies. One-way coupling, which transfers pressure data from CFD solvers to structural models without feedback, offers an efficient approach for initial assessments and has been used effectively in studies such as those by Takami et al. [15-17] to predict global and local hydroelastic responses of ships in waves. In contrast, two-way coupling methods, such as those proposed by Xiao et al. [18] and Lu et al. [19], enable dynamic interaction between fluid and structural solvers, leading to more accurate predictions of slamming loads and transient stress concentrations. In the context of planing hulls and ship-like wedge sections, numerous experimental and numerical efforts have been carried out. For instance, Alexandru et al. [20] provided benchmark data on slamming loads for ship-like sections, while Paik et al. [21] and Maki et al. [22] applied strongly coupled FSI methods to analyze structural loads on surface ships and stern structures under impact events. These works highlight the nonlinear nature of wave impact and the importance of including hydroelastic effects in stress evaluations. Further, Jiao et al. [23, 24] and Chen et al. [25] explored springing and whipping responses of flexible hulls using partitioned CFD-FEM methods, demonstrating the capability of such approaches in capturing complex fluid dynamics, including wave breaking, air entrapment, and localized pressure peaks. Liang et al. [26] extended this work to marine propellers, emphasizing the broad applicability of fluid-structure coupling in maritime design optimization. In terms of structural failure prediction, recent advancements by Liu et al. [27] proposed numerical simulations for collapse behavior of large container and bulk carriers under extreme wave conditions, integrating nonlinear FEA with real-time wave loads derived from CFD simulations. While the computational cost of two-way coupling remains a concern, researchers such as Rainald et al. [28] and Takami et al. have also worked to extend the practical range of one-way coupling, showing its reliability when properly validated. Furthermore, review studies such as Li et al. [29] have provided comprehensive evaluations of CFD-FEM strategies, suggesting that hybrid approaches can balance computational cost and accuracy.

Based on this background, the present study adopts a one-way coupled CFD-FEA method to investigate the structural behavior of a high-speed planing hull under calm water and wave conditions. Critically, CFD-calculated dynamic pressures (rather than empirical estimates) directly drive the structural analysis to ensure physics-based accuracy. By focusing on displacement, semi-planing, and planing navigation states, and simulating both hogging and sagging stress profiles, the method seeks to provide a more precise and localized assessment of hull bottom pressures. Comparison with empirical design methods further reveals the strengths of the CFD-based approach in capturing real-world stress distributions, particularly nonlinear slamming effects unique to planing hulls. Ultimately offering a reliable framework for structural strength evaluation and optimization in planing hull design.

2. Numerical method

2.1 Fluid flow governing equations

The flow of fluids must adhere to the fundamental laws of conservation, which are categorized into three types: conservation of mass, momentum, and energy. For a general compressible Newtonian fluid, these conservation laws can be expressed using the following control equations.

Conservation of Mass:

$$\frac{\partial \rho_f}{\partial t} + \nabla \cdot \left(\rho_f v \right) = 0 \tag{1}$$

Conservation of Momentum:

$$\frac{\partial \rho_f v}{\partial t} + \nabla \cdot \left(\rho_f v v - \tau_f \right) = f_f \tag{2}$$

where t is the time, f_f is the body force vector, ρ_f is the fluid density, v is the fluid velocity vector, τ_f is the shear stress tensor, expressed as:

$$\tau_f = \left(-p + \mu \nabla \cdot v \right) I + 2\mu e \tag{3}$$

where p is the fluid pressure, μ is the dynamic viscosity, I is the identity tensor, e is the velocity gradient tensor, defined as:

$$e = \frac{1}{2}\left(\nabla v + \nabla v^T \right) \tag{4}$$

2.2 Structural governing equations

According to Newton's second law, the momentum conservation equation for the solid domain can be expressed as:

$$\rho_s \ddot{d}_s = \nabla \cdot \sigma_s + f_s \tag{5}$$

where ρ_s is the solid density, σ_s is the Cauchy stress tensor, f_s is the body force vector, $\ddot{d}_s$ is the acceleration vector within the solid domain.

2.3 One-way coupled method

After completing the CFD calculation, the pressure load can be transferred from the CFD fluid flow module (Fluent) to the static structural module for FEM analysis. CFD was performed in ANSYS Fluent 2023 R1, and the pressure fields were transferred to the Static Structural module in ANSYS Workbench 2023 R1 for FEA. This implements a one-way coupled approach wherein CFD-derived pressures unidirectionally drive FEA, without structural deformation feedback to the fluid domain. The analysis workflow for one-way fluid-structure coupling is shown in Figure 1.

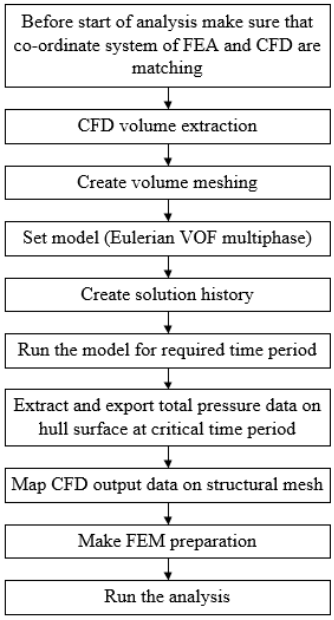

Fig. 1 One-way fluid-structure coupling analysis workflow

3. Numerical model

3.1 Subject ship

Full-scale CFD/FEA models were employed to avoid scaling uncertainties in fluid impact and structural responses. The main parameters of the planing hull analyzed in this study are summarized in Table 1.

Table 1 Principal particulars of the subject ship

Main Feature	Value
Length overall	12.50 m
Beam overall	3.30 m
Depth	1.60 m
Draft	0.70 m
Length waterline	11.50 m
Displacement	17.00 t

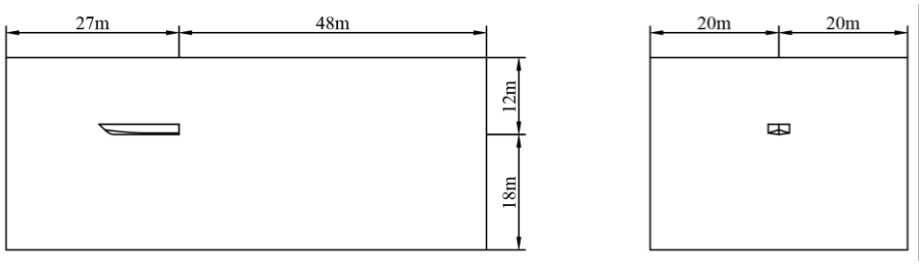

(a) Length and height of the computational domain (b) Width of the computational domain

Fig. 2 Basic dimensions of the computational domain

3.2 CFD model

The computational domain with appropriate dimensions was defined according to the length of the hull, as shown in Figure 2. The front extends 14.5 m forward from the bow, the rear extends 48 m aft from the stern, the upper boundary extends 12 m above the baseline, the lower boundary extends 18 m below the

baseline, and the sides extend 20 m from the centerline in both directions. To ensure the complete transmission of the hull bottom load during the finite element calculation, a full-ship model was used for the numerical simulation.

Due to the rapid transition of the hull bottom surface, a hybrid grid method was used for mesh generation. The hull model is enclosed by a cube in the central region, Figure 3. This region was meshed with an unstructured grid to ensure good surface fitting, while the external region used structured grids. Additionally, the mesh around the hull and the waterline region was refined to enhance the capture of wave-making effects. A boundary layer was set to achieve a y^+ value of approximately 10 on the hull surface. The total number of volume cells in the computational domain was approximately 3 million.

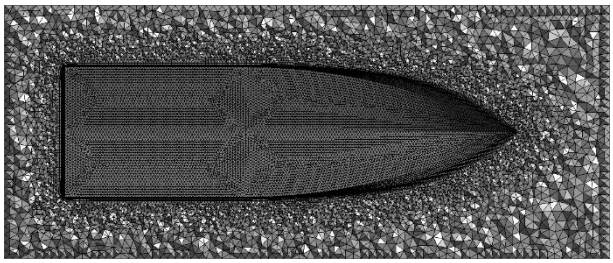

Fig. 3 Hull mesh distribution

The boundary conditions for the computational domain are shown in Figure 4. The front boundary is a velocity inlet, the rear is a pressure outlet, the sides are symmetric boundaries, and the top and bottom, as well as the hull surface, are treated as wall boundaries. The volume of fluid (VOF) model based on geometric reconstruction technology was used to capture the water-air interface, and the k-ω SST turbulence model was applied.

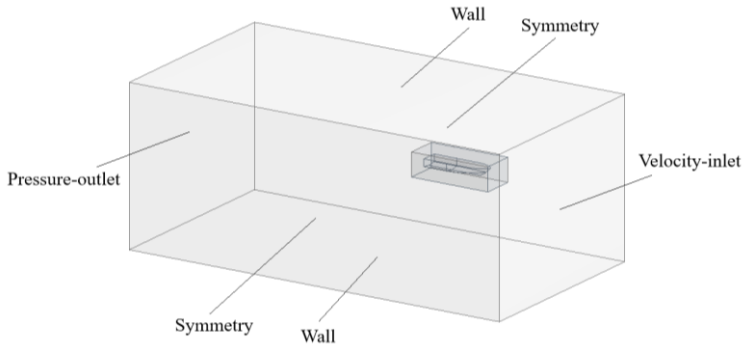

Fig. 4 Boundary conditions of the computational domain

3.3 FE model

A Cartesian coordinate system was used for modeling, with the origin located at the intersection of the stern plate and the baseline of the hull. The X-axis points from the stern to the bow along the length of the ship, the hull bottom plate lies in the XY plane, and the Z-axis is along the ship's height. For the structural analysis, a full-ship model was used, which includes all the hull outer plates, decks, bulkheads, main support components, and superstructure. Within ANSYS Workbench, shell elements (employing the default SHELL181 formulation) modeled plates and stiffener webs, while beam elements (BEAM188 formulation) modeled stiffener flanges and longitudinal/transverse members, Figure 5. Stress singularities at corners were mitigated by mesh refinement and averaging nodal stresses over adjacent elements. The complete model comprised 77,949 elements with 76,854 nodes.

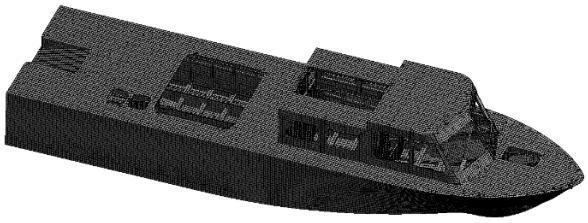

Fig. 5 Finite element model

The materials used for the planing hull structure are all aluminum alloys, with the main hull outer plates made of 5059 aluminum alloy, the remaining plates made of 5083 aluminum alloy, and the structural members made of 6082 aluminum alloy. The material properties are shown in Table 2.

Table 2 Hull material properties

Model	Young's Modulus (E)	Poisson's Ratio (μ)	Density (ρ)
5083 Aluminum Alloy	7.1×10^4MPa	0.33	2.67×10^3kg/m^3
5059 Aluminum Alloy	7.1×10^4MPa	0.33	2.75×10^3kg/m^3
6082 Aluminum Alloy	7.03×10^4MPa	0.35	2.70×10^3kg/m^3

In the finite element strength evaluation, Inertia Relief boundary conditions were applied, with six degrees of freedom constrained at a node near the neutral axis of the hull.

4. Numerical setup

4.1 Grid independence analysis

Before analyzing the structural strength of the planing hull, a grid independence study was conducted based on the pressure distribution along the hull bottom. The calm semi-planing condition was selected as the test case, and calculations were performed using coarse (1.5 million cells), medium (3 million cells), and fine (6 million cells) mesh densities. Figure 6 illustrates the pressure distribution curves along the mid-longitudinal section of the hull bottom.

From the results, it was found that when the grid density was 1.5 million, the pressure coefficient curve deviated significantly from the curves of the higher-density grids, especially in the negative pressure region at the stern and the water impact region at the bow. When the number of grid elements exceeded 3 million, the pressure distribution showed little change with further increases in grid density, indicating that refining the mesh did not significantly improve the accuracy of the results. Considering both the computational accuracy and resource cost, the medium grid was chosen as the optimal grid for structural strength evaluation of the planing hull based on the hydrodynamic method.

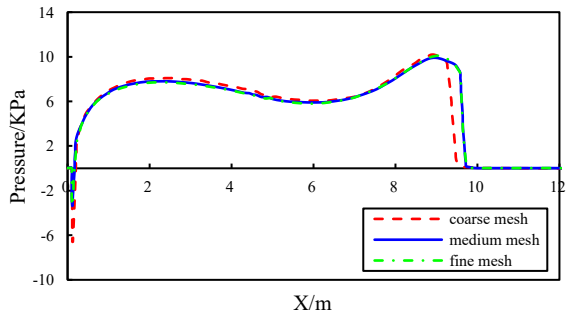

Fig. 6 Pressure distribution along the mid-longitudinal section of the hull bottom for different mesh densities

4.2 Model testing verification

The scale ratio of this boat model is 1:4. The resistance and flotation characteristics at different speeds were obtained through experiments. This section analyzes the resistance and wave-making characteristics of the planing hull at Fr_∇ ranging from 1.03 to 3.10 using numerical simulations, comparing them with the model test results to verify the accuracy of the flow field simulation. The test navigation posture at corresponding speeds was used as the boundary condition for the numerical simulations.

As shown in Figure 7, the trend of the drag-lift ratio obtained from the numerical simulation closely matches that from the model tests. As the speed increases, the hull resistance first increases and then decreases. At low speeds, the error between the two is small, about 8.95 %, but once the hull enters the semi-planing state, the numerical resistance is higher, with an error of 16.15 %. However, at higher speeds, the error decreases to 10.53 %, and the trend of the drag-lift ratio in the numerical simulation aligns well with the test results.

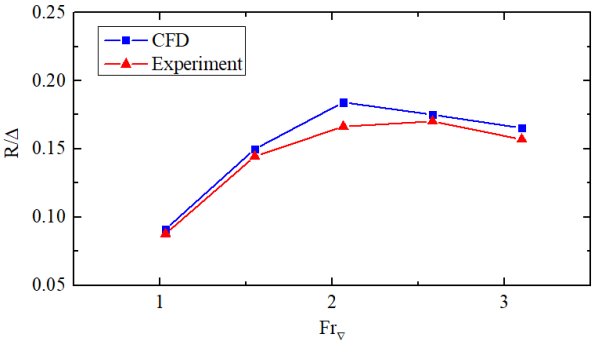

Fig. 7 Drag-lift ratio curve

At $Fr_\nabla = 3.10$, after entering the planing state, the longitudinal tilt angle decreases relative to the semi-planing state, and the hull experiences significant lift. The wave-making splash point on both sides of the bow moves from the bow to the midship, while the wetted area at the stern decreases due to the hull lift. From the model tests, it can be seen that the splash on both sides has transitioned from a water film to a jet-like spray, and the stern vortex is longer and deeper.

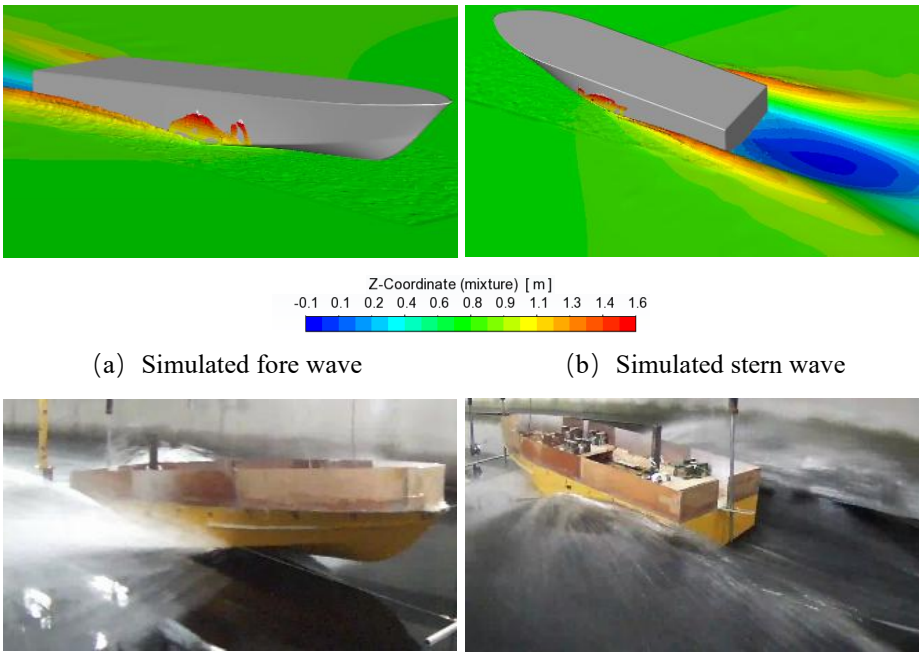

(a) Simulated fore wave (b) Simulated stern wave

(c) Experimental fore wave (d) Experimental stern wave

Fig. 8 Comparison of simulated and experimental wave-making (calm water, $Fr_\nabla = 3.10$)

Comparing the wave-making results (Figure 8) from the tests and the numerical simulation, it can be observed that the CFD method provides a good simulation of the main spray, but the simulation of the water mist after the spray dispersion is less accurate. This is mainly due to the limitations of grid scale and the VOF method. While the CFD results show less fine spray compared to the experiment, the primary impact features, jet formation, pressure footprint, and flow angle are in good agreement. The discrepancy arises from unresolved sub-grid secondary droplet breakup. However, the wave-making on both sides of the hull and the stern vortex were captured well. Overall, the CFD numerical method was able to accurately simulate the wave-making characteristics of this planing hull.

5. Calculation and loading of the empirical load

5.1 Total strength calculation load

According to the relevant requirements in the standard [30], the overall load for the total strength calculation is composed of static loads and wave loads. The static loads include the gravity and hydrostatic uplift in the fully loaded departure state, which can be directly determined using the empirical calculation method. The wave load for high-speed hulls is typically determined by ship model testing. In the absence of model test data, the wave load can be determined using the following formula. Here, it is assumed that the total longitudinal bending moment of the hull is distributed along the length of the ship according to a cosine curve:

$$M(x)=\frac{M_{BY}}{2}\left(\cos\left(\frac{x}{L}2\pi\right)\text{-}1\right) \tag{6}$$

where x is the longitudinal coordinate of the cross-section starting from the origin, M_{BY} is the total longitudinal bending moment at the hull's transverse cross-section. The calculation of M_{BY} should be carried out under two distinct conditions, as described below.

5.2 Total longitudinal bending moment in displacement state

When a high-speed hull is in the displacement state, its total longitudinal bending moment can be determined by adding the still water bending moment and the wave-induced bending moment to calculate the hogging and sagging moments:

$$M_{BY}=M_C+M_W \tag{7}$$

where M_C is the bending moment when the ship is at rest in calm water, M_W is the wave-induced bending moment when the ship is exposed to waves.

The wave-induced bending moment is determined based on the maximum significant wave height in the operational region, with the assumption that the wavelength equals the ship's length. The wave parameters include wave shape, wavelength, and wave height. The most commonly used theory is the Timoshenko wave theory, where the profile of the two-dimensional wave is a Timoshenko curve, characterized by steep crests, flat troughs, and unequal areas above and below the wave axis, hence the name "Timoshenko wave." The wave surface equation for Timoshenko waves is:

$$\begin{cases} x=\dfrac{\lambda}{2\pi}\theta+r\sin\theta \\ y=\text{-}r\cos\theta \end{cases} \tag{8}$$

where x is the vertical coordinate from the wave axis, y is the horizontal coordinate along the wave axis, λ is the wavelength, r is the half-wave height.

Based on the operational limitations, the maximum significant wave height $H_{1/3\max}$ that a ship operating in sheltered areas may encounter should not exceed 2.0m. Therefore, we take $r=1.0m$, and $\lambda=11.5m$, to obtain the wave height curve as shown in Figure 9.

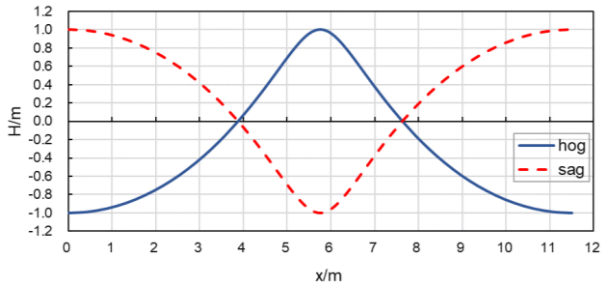

Fig. 9 Wave height curve

5.3 Total longitudinal bending moment induced by wave impact

For all types of high-speed vessels, except for the full-cushion air-cushion vessels, the total longitudinal bending moment M_{BY} induced by wave impact can be calculated using the following formula:

$$M_{BY}=C_1C_2C_3(1+n)\left(l_x\text{-}0.175\frac{\Delta}{B_s d}(1+0.2n)\right)\Delta g \tag{9}$$

where C_1 is the coefficient for hogging, with $C_1=1.0$, and for sagging, $C_1=\text{-}1.0$. C_2 is the coefficient, set at $C_2=0.5$, and C_3 is the ship-type coefficient, with $C_3=1.00$. n is the overload coefficient, is defined as $n=a_{cg}/g$, where a_{cg} is the vertical acceleration at the center of gravity. l_x is the longitudinal distance between the forward and aft centers of gravity, with an approximate value of $l_x=0.25L$. B_s is the width of the impact area on the hull bottom when the wave crest impacts the midship bottom area. For sharp bow ships, B_s can be taken as the horizontal distance from the chine to the centerline of the hull.

For this hull, considering personnel comfort as a working ship, a_{cg} is taken as $1.3g$. The total longitudinal bending moment induced by wave impact can be equivalently loaded by applying a vertical force $q(x)$ distributed along the length of the ship. $q(x)$ can be calculated using the following formula:

$$q(x)=A\cos\left(\frac{x}{L}2\pi\right) \tag{10}$$

where A is defined as $\dfrac{2\pi^2 M_{BY}}{L^2}$.

By changing the direction of the vertical force, equivalent uniformly distributed loads for both hogging and sagging conditions can be calculated, as shown in Figure 10. On the structural model, a vertical force $q(x)$ is distributed along the length of the ship, or an equivalent concentrated force, can be applied to achieve the equivalent loading of the total longitudinal bending moment.

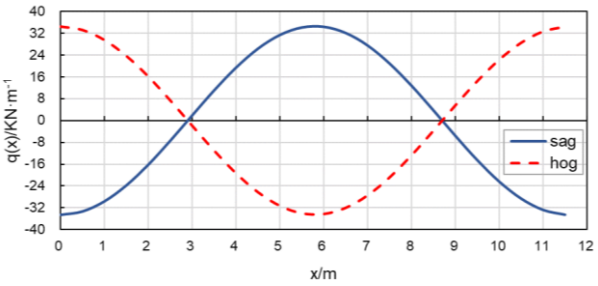

Fig. 10 Equivalent uniformly distributed load

5.4 Standard Formula Total Strength Check Results

Under displacement navigation conditions, the additional wave bending moment is equivalently applied through variable-height hydrostatic pressure. In the sagging condition, the bow and stern experience significant pressure, resulting in notable deformation at the bow keel and the bilge near the pump compartment. The maximum von-Mises stress (Figure 11) in the plate elements is observed at the keel in the bow compartment, with a value of 26.162 MPa. In contrast, under hogging conditions, the planing hull undergoes hogging deformation due to bilge water pressure, with the maximum stress of 24.387 MPa concentrated in the midship bottom panel. Additionally, significant stress is observed along the deck edge of the bilge due to hull bending.

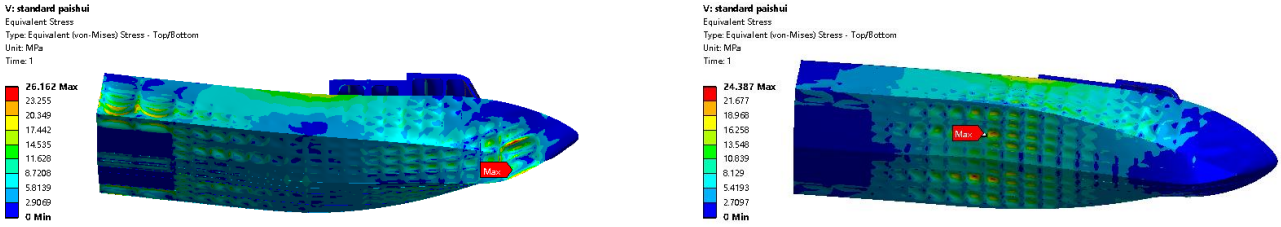

(a) Sagging (b) Hogging

Fig. 11 Plate von-Mises stress for the planing hull in displacement navigation state

In the high-speed navigation state, due to the fact that the hull bottom structure is larger than the deck structure and the neutral axis is closer to the hull bottom, the planing hull undergoes a sagging deformation under the action of the total longitudinal bending moment in the sagging condition. The top of the hull side deck is compressed, and the maximum von-Mises stress is 33.36 MPa, as shown in Figure 12(a). In the hogging condition, the maximum stress similarly occurs at the top of the hull side deck, but this time the stress is tensile. The maximum von-Mises stress is 32.324 MPa.

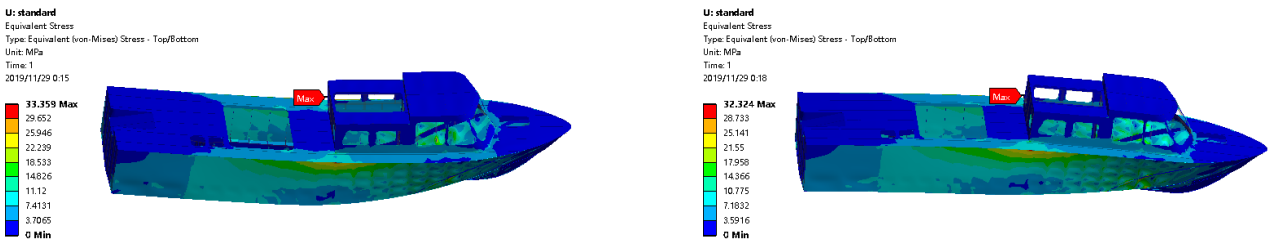

(a) Sagging (b) Hogging

Fig. 12 Plate von-Mises Stress for the planing hull in high-speed navigation state

According to the relevant requirements in the rules [30] for directly calculating the structural strength of aluminum alloy high-speed hulls, the stresses in each component during the total strength calculation should not exceed the allowable stresses listed in Table 3.

Table 3 Allowable stress for total strength

	Aluminum alloy structure
Allowable equivalent stress for plate elements (MPa)	$0.75\sigma_{SW}$ =0.75×125= 93.75Mpa
Allowable shear stress for plate elements (MPa)	$0.41\sigma_{SW}$ =0.41×125=51.25Mpa
Allowable normal stress for beam and rod elements (MPa)	$0.73\sigma_{SW}$ =0.73×115=83.95Mpa

The σ_{SW} of aluminum alloys before and after welding varies. The yield strengths of 5059 and 5083 plates before and after welding are 215/125 MPa, and the yield strengths of 6082 materials are 240/115 MPa.

The maximum stresses for the plate and beam elements in each condition are shown in Table 4. It can be seen that the maximum plate stress, shear force, and beam stress of the planing hull all meet the requirements of the rules.

In the displacement navigation condition, the maximum stress in the plate elements occurs at the pressure peak of the wave-induced bending moment. In the hogging condition, the maximum stress is concentrated in the midship, while in the sagging condition, the stress is distributed across the bow and stern. In contrast, in the high-speed navigation condition, the hull's maximum stress is higher. The peak stress in the plate elements mainly occurs at the top of the hull side deck. Since this position is close to the main deck and far from the neutral axis, the impact of the hogging and sagging conditions on the hull is more significant when the load is evenly distributed.

Table 4 Structural stress calculation results

Condition		Maximum plate stress	Maximum plate shear stress	Maximum beam stress	Verification result
Displacement navigation	Sagging	26.162 MPa	12.446 MPa	14.949 MPa	Satisfy
	Hogging	24.387 MPa	7.759 MPa	5.095 MPa	Satisfy
High-speed navigation	Sagging	33.359 MPa	10.061 MPa	8.035 MPa	Satisfy
	Hogging	32.324 MPa	8.722 MPa	7.458 MPa	Satisfy

6. Hydrodynamic-based total strength evaluation of the planing hull

6.1 Calm water navigation strength evaluation results

Deck and superstructure stresses remain below bottom plate maxima due to the absence of direct hydrodynamic loading. Therefore, bottom and side stress distributions are prioritized for visualization. When $Fr_{\nabla}=1.03$, the planing hull operates in a displacement mode. As observed in Figure 16(a), the maximum von Mises stress of the plate elements (8.92 MPa) occurs along the chine at the bow, where the flow pushes the water to form waves, resulting in significant dynamic pressure. In the semi-planing mode at $Fr_{\nabla}=2.06$, the pitch angle of the craft increases, causing the wave impact point at the bow to shift backward. Consequently, the maximum von Mises stress of the plate elements (15.379 MPa) occurs at the bottom of the cabin. At $Fr_{\nabla}=3.10$, during planing, the hull lifts and partially departs from the water, leading to a significant reduction in draft at the stern legs. Stress concentrations on both sides of the pump chamber disappear, and the high-stress region of the hull shifts from the entire bottom area to the "V"-shaped forward-flow region in the middle of the bottom. The maximum von Mises stress of the plate elements (31.42 MPa) is found in this region. Additionally, stress concentration zones (approximately 10 MPa) emerge on both sides of the bow deck, indicating that the structural integrity demands of the hull are higher during planing conditions. Under planing conditions ($Fr_{\nabla}=3.10$), the pressure distribution exhibits strong nonlinearity due to air entrapment and water separation. As depicted in Figure 13(f), the localized high-pressure zone at the midship "V"-shaped region correlates with stress concentration (31.42 MPa), demonstrating CFD's capability to resolve critical dynamic loads.

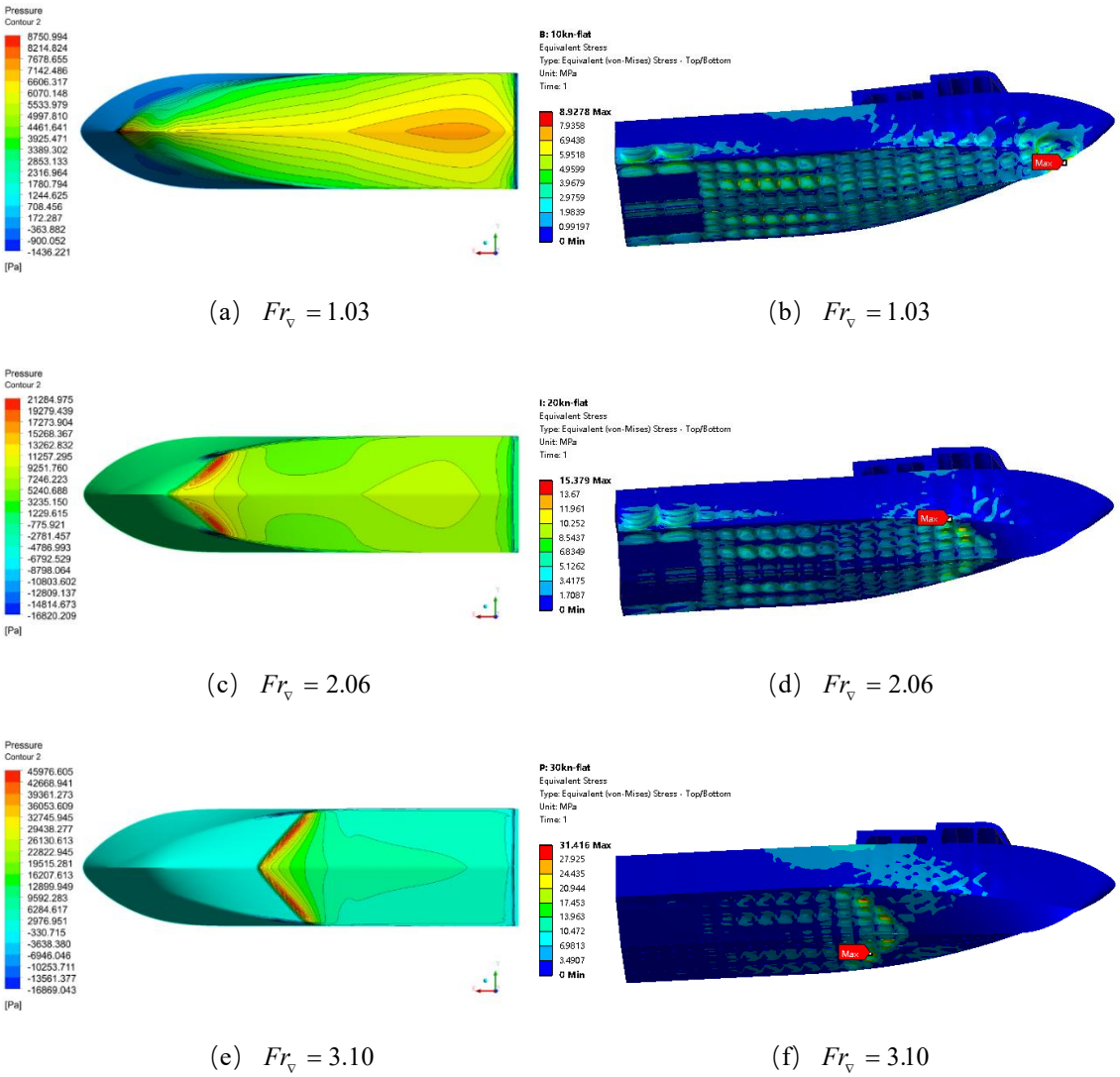

Fig. 13 Hull bottom pressure distribution and plate von-Mises stress (calm water)

Under calm water conditions, the maximum structural stresses for the three speeds, are shown in Table 5. The maximum stress approximately doubles under the three speeds. Consequently, the hull's structural strength fully meets the requirements for calm water navigation.

Table 5 Structural stress calculation results

Condition	Maximum plate stress	Maximum plate shear stress	Maximum beam stress	Verification result
Displacement state	8.928 MPa	3.948 MPa	2.850 MPa	Satisfy
Semi-planing state	15.379 MPa	5.466 MPa	4.010 MPa	Satisfy
Planing state	31.416 MPa	10.130 MPa	5.430 MPa	Satisfy

6.2 Planing hull wave navigation strength evaluation results

Numerical waves are generated using Fluent's Open Channel Flow, and transient calculations are employed to simulate the planing hull's navigation state under hogging and sagging conditions. The hydrodynamic characteristics of the craft in waves were analyzed. When the planing hull navigates in waves, the wave impact generally limits its maximum speed in specific sea conditions. This not only considers

personnel comfort but, more importantly, ensures structural safety. According to the rules, the relationship between the significant wave height $H_{1/3}$ and navigation speed V_H is given by the following equation:

$$a_{cg} = \frac{1}{426}\left(\frac{V_H}{\sqrt{L}}\right)^{1.4}\left(\frac{H_{1/3}}{B_{wl}}+0.07\right)(50-\beta)\left(\frac{L}{B_{wl}}-2\right)\frac{B_{wl}^{\ 3}}{\Delta}g \tag{11}$$

where g is the gravitational acceleration, a_{cg} is the vertical acceleration at the center of gravity, V_H is the ship's speed when the wave height is $H_{1/3}$, $H_{1/3}$ is the significant wave height, L is the ship's length, B_{WL} is the waterline breadth, β is the hull's bottom slant angle at the transverse cross-section corresponding to the center of gravity, Δ is the full-load displacement.

For this hull, the vertical acceleration a_{cg} is taken as $1.3g$. Correspondingly, the significant wave height $H_{1/3}$ for the planing hull at different speeds V_H can be calculated. Additionally, based on the operational restriction levels, the maximum significant wave height $H_{1/3\max}$ that a ship operating in sheltered areas may encounter should not exceed 2.0m. The following navigation conditions, which are based on these criteria, are summarized in Table 6.

Table 6 Wave navigation conditions

Condition	Fr_∇	Speed	Wavelength	Wave height
Displacement state	1.03	10 kn	11.5 m	2.00 m
Semi-planing state	2.06	20 kn	11.5 m	1.15 m
Planing state	3.10	30 kn	11.5 m	0.55 m

For wave conditions, pressure fields at hogging/sagging instants (corresponding to wave crest/trough amidships) were extracted to match empirical load cases defined in Section 5. Under three navigation states, the loading characteristics of the planing hull exhibit significant differences between hogging and sagging conditions. As shown in Figures 14(a) and (b), during displacement mode, sagging conditions cause water to accumulate at the stern, resulting in maximum pressure concentration along both sides of the bilge pump chamber. The maximum von-Mises stress in the plate elements reaches 13.846 MPa. In contrast, under hogging conditions, the wave crest is compressed by the hull bottom, leading to a more uniform pressure distribution, with the maximum von-Mises stress reduced to 10.12 MPa at the engine room bottom.

In the semi-planing state, as depicted in Figures 14(e) and (f), sagging conditions lead to localized pressure concentration at the bow where it interacts with the wave crest, generating a maximum von-Mises stress of 19.83 MPa. Conversely, under hogging conditions, the bow rises, shifting the impact zone aft to the rear hull bottom. The affected area increases, the stress decreases, with the maximum von-Mises stress dropping to 8.59 MPa, also located at the engine room bottom.

In the planing state shown in Figure 14(i), under sagging conditions, the maximum pressure point on the hull bottom shifts slightly aft compared to still-water conditions, with a reduction in wetted area. The peak von-Mises stress in the plate elements reaches 17.47 MPa, concentrated at the engine room bottom. Under hogging conditions, the wetted area increases, and the impact zone shifts forward to the bilge chine area. The maximum von-Mises stress is 14.78 MPa, distributed along the bilge chine.

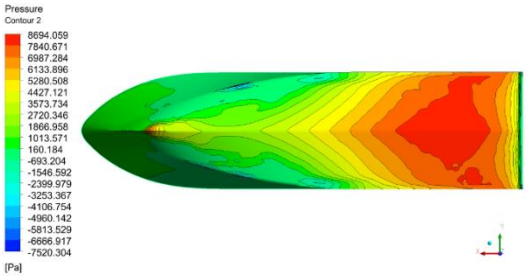

(a) Sagging, $Fr_{\nabla} = 1.03$

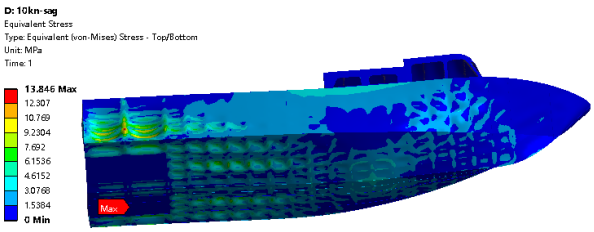

(b) Sagging, $Fr_{\nabla} = 1.03$

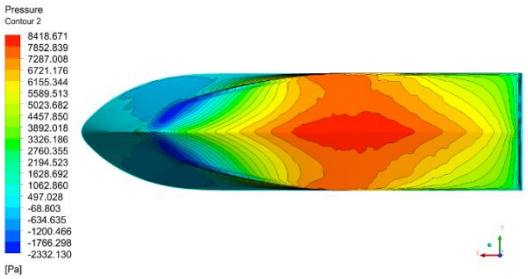

(c) Hogging, $Fr_{\nabla} = 1.03$

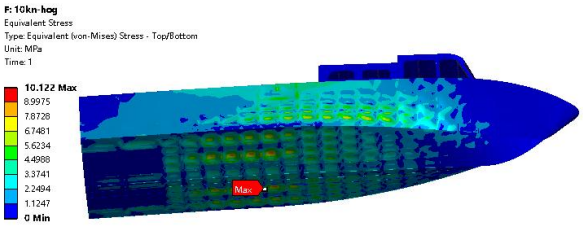

(d) Hogging, $Fr_{\nabla} = 1.03$

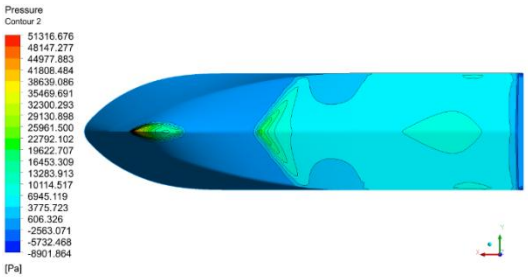

(e) Sagging, $Fr_{\nabla} = 2.06$

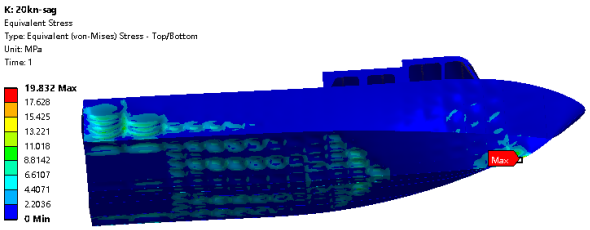

(f) Sagging, $Fr_{\nabla} = 2.06$

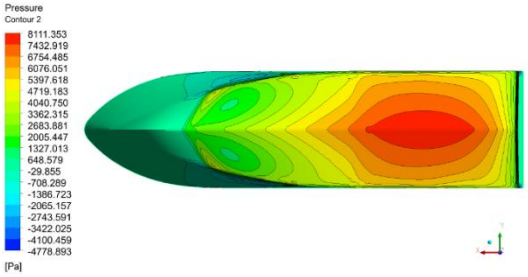

(g) Hogging, $Fr_{\nabla} = 2.06$

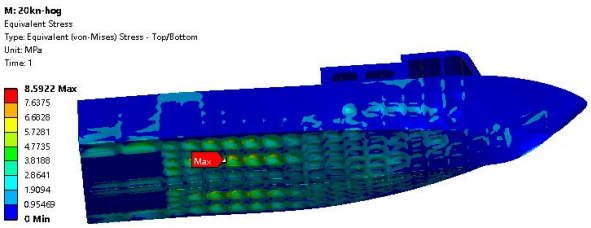

(h) Hogging, $Fr_{\nabla} = 2.06$

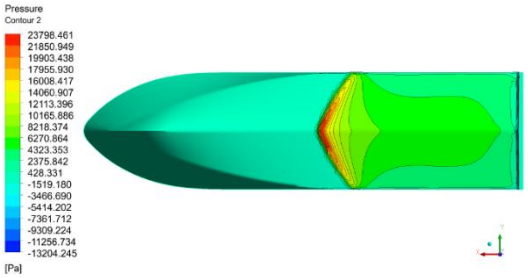

(i) Sagging, $Fr_{\nabla} = 3.10$

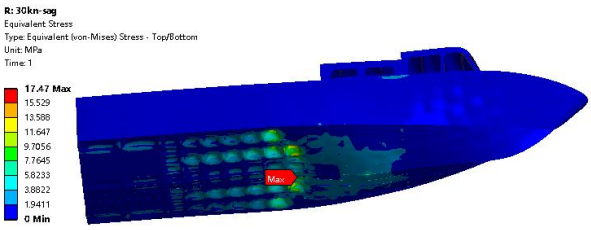

(j) Sagging, $Fr_{\nabla} = 3.10$

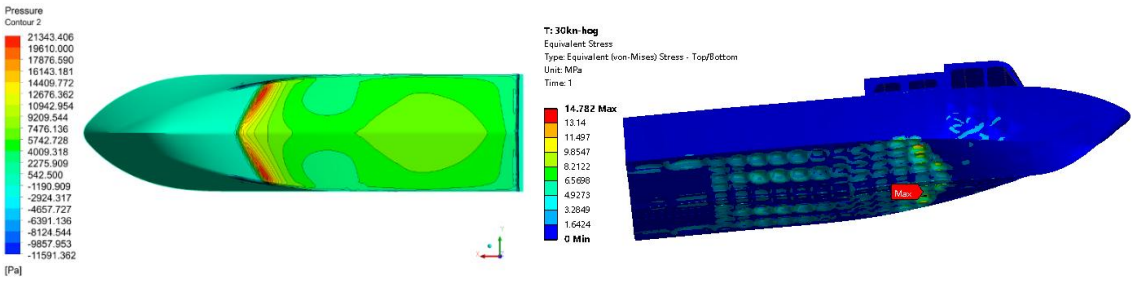

(k) Hogging, $Fr_{\nabla} = 3.10$ (l) Hogging, $Fr_{\nabla} = 3.10$

Fig. 14 Hull bottom pressure distribution and plate von-Mises stress (wave water)

6.3 Analysis of curve stress results

To analyze the longitudinal distribution of von-Mises stress on the hull bottom, three target lines were selected across the bottom region, as shown in Figure 15. Corresponding bottom plate pressure distributions are provided in Figure 14. These include the intersection of the keel and the bottom plate along the centerline (A-A curve) and the intersections of the side keels with the bottom plate (B-B and C-C curves). Due to the symmetric stress distribution along the Y-axis in both hogging and sagging conditions, only the stress curves on one side were analyzed.

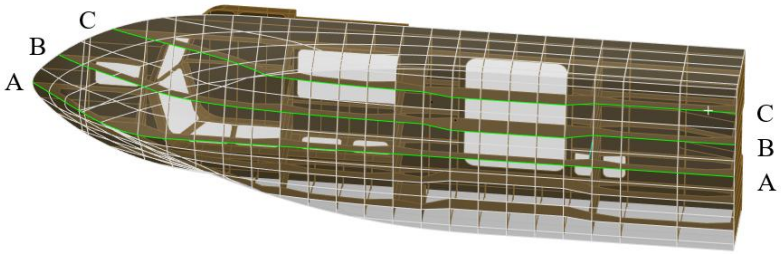

Fig. 15 Schematic of curve stress extraction

Figure 16 illustrates the stress distribution along the ship's longitudinal direction under sagging conditions. In the displacement state, the stress along the girder bottoms is relatively uniform, with higher stress observed at the stern due to concentrated hydrostatic pressure from deep immersion (Figure 14(a)). Additionally, the stress exhibits periodic variations along the ship length, attributed to the structural support of the internal frames, with higher stress occurring between frames. In the semi-planing state, as shown in Figure 16(a), the A-A curve shows stress peaks near the bow, this results from bow-flare slamming: water impact generates localized pressure spikes (Figure 14(e)). In the planing state, as depicted in Figures 16(b) and (c), the maximum stress is located approximately 5 meters aft of the transom. This correlates with the "V-bottom spray root impact zone" (Figure 14(j)), where dynamic pressures due to fluid stagnation. The corresponding bottom plate pressure distribution is comprehensively visualized in Figure 14, revealing direct causality between local pressure peaks and structural stress concentrations.

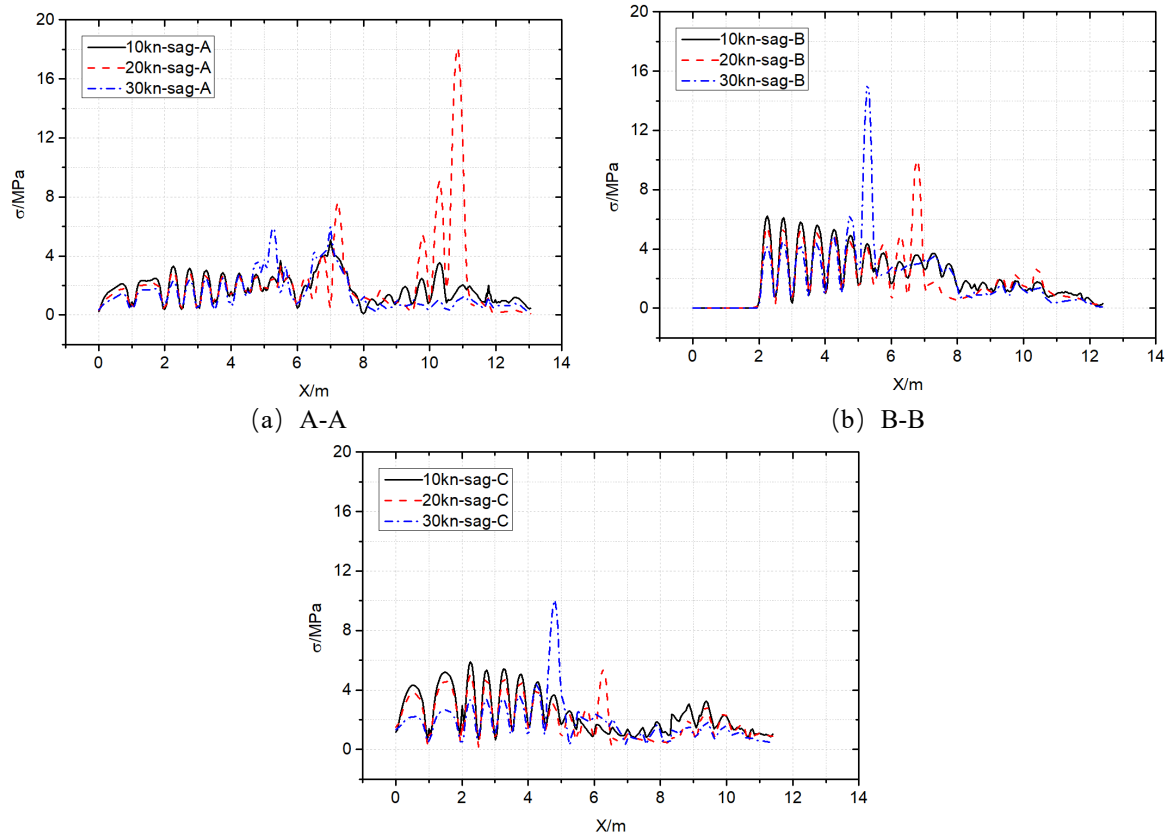

(a) A-A (b) B-B

(c) C-C

Fig. 16 Equivalent stress distribution along the hull length (sagging)

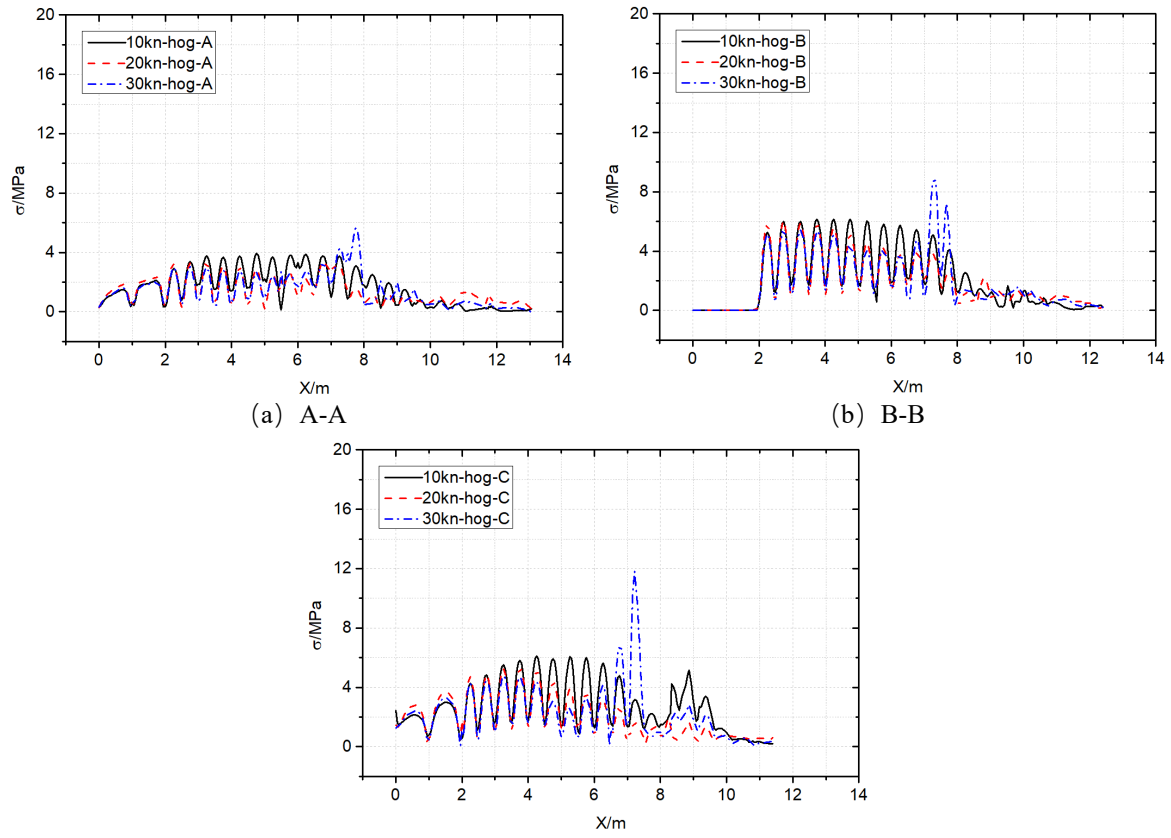

(a) A-A (b) B-B

(c) C-C

Fig. 17 Equivalent stress distribution along the hull length (hogging)

In hogging conditions, the keel-bottom stress distribution is relatively uniform in both displacement and semi-planing states, showing periodic variations corresponding to frame spacing, particularly pronounced in the aft hull where reduced frame density increases unsupported spans (Figure 17). Unlike sagging, where water flow induces localized stress concentrations, high-stress regions in hogging appear only in the planing state, primarily at midship near the sides due to chine-spray root impacts generating concentrated pressures (Figure 14(l)). Overall, stress levels under hogging remain lower than those in sagging as hull bottom disengagement reduces hydrodynamic loading. As indicated by the A-A and B-B curves, the bow bottom is largely unaffected by water impact in hogging with the bow aerated and clear of water, with minor stress increases along the C-C curve only in the planing state, attributable to spray jet side-loading (Figure 14(k)).

The results in Table 7 indicate that the maximum von-Mises stress, shear stress of the plate elements, and the maximum stress of the beam elements under hogging and sagging conditions across three navigation states all meet the requirements of the rules. The numerical simulation not only provides a direct verification of the global strength of the planing hull but also delivers precise analyses of local high-stress regions, such as the hull bottom and side plating, offering critical insights for design optimization.

Table 7 Structural stress calculation results

Condition		Maximum Plate Stress	Maximum Plate Shear Stress	Maximum Beam Stress	Verification Result
Displacement state	Sagging	13.846 MPa	5.486 MPa	7.511 MPa	Satisfy
	Hogging	10.122 MPa	3.061 MPa	2.640 MPa	Satisfy
Semi-planing state	Sagging	19.832 MPa	9.126 MPa	6.958 MPa	Satisfy
	Hogging	8.592 MPa	2.892 MPa	1.812 MPa	Satisfy
Planing state	Sagging	17.470 MPa	5.605 MPa	2.674 MPa	Satisfy
	Hogging	14.782 MPa	4.578 MPa	3.094 MPa	Satisfy

7. Comparative analysis of total strength check results

Empirical wave loads serve solely as a regulated baseline to validate CFD's superiority in capturing localized effects. This section compares the total strength check results from the standard formula method (Table 8) and the hydrodynamic method (Table 9), focusing on the maximum stress in the plate elements. The hydrodynamic method yields a maximum plate stress of 31.416 MPa in calm water conditions, which is only 5.82 % lower than the 33.359 MPa obtained from the standard formula method. In the wave conditions, however, the maximum stress calculated using the hydrodynamic method is significantly lower. The maximum stress, which occurs in the semi-planing condition under sagging waves, is 19.832 MPa, which is 36.87 % lower than the value in calm water conditions. This indicates that the hogging and sagging wave conditions are not the most critical conditions for the planing hull's strength during wave navigation, as their effects on the hull's total strength are much smaller than those on displacement hulls. The standard formula method calculates higher stresses, mainly because it includes the consideration of wave impact forces, thus providing a higher safety margin.

From a comparison of the maximum stress positions, the standard formula method calculates the maximum stress at the midship side plates using equivalent bending moments. However, in reality, the planing hull does not experience such large total longitudinal bending moments during wave navigation due to its different navigation state from a displacement hull. The maximum stress calculated by the hydrodynamic method occurs at the midship hull bottom, where the hull is continuously impacted by water flow, and this area should be given more attention in structural strength considerations.

Table 8 Standard formula method check results

Condition		Maximum plate stress
Displacement navigation	Sagging	26.162 MPa
	Hogging	24.387 MPa
High-Speed navigation	Sagging	33.359 MPa
	Hogging	32.324 MPa

Table 9 Hydrodynamic method check results

Condition			Maximum plate stress
Calm water	Displacement state		8.928 MPa
	Semi-Planing state		15.379 MPa
	Planing state		31.416 MPa
Wave water	Displacement state	Sagging	13.846 MPa
		Hogging	10.122 MPa
	Semi-planing state	Sagging	19.832 MPa
		Hogging	8.592 MPa
	Planing state	Sagging	17.470 MPa
		Hogging	14.782 MPa

8. Conclusions

This study focuses on a 12-meter high-speed planing hull using a single-phase fluid-structure coupling method based on CFD and FEA to evaluate the structural strength of the planing hull under different navigation states and wave conditions. The methodology demonstrates potential advantages over conventional empirical methods through high-fidelity resolution of localized phenomena. Comparative analysis with standard formula-based results yields the following observations:

(1) The standard formula method, while indicating that the planing hull's total longitudinal strength meets the requirements, fails to accurately reflect the distribution of local loads at the hull bottom under wave impact. For instance, the maximum stress was calculated to occur at the midship side plates, which does not align with the actual high-stress areas, suggesting limited applicability for non-standard hull forms.

(2) The CFD-based wave load calculation method effectively captures complex nonlinear phenomena, such as free surface breaking and splashing. This method provides a more accurate hull bottom pressure distribution, particularly in the planing state, with the maximum stress occurring at the midship hull bottom, which is consistent with the actual stress characteristics of the planing hull.

(3) The calm water planing state presents the most critical condition for the planing hull, with the maximum stress being only 5.82% less than that obtained using the standard formula method. Numerical simulations reveal a more precise local stress distribution at the hull bottom, which is crucial for structural design.

(4) The combined CFD and FEA approach not only accurately determines the total longitudinal strength of the planing hull but also offers a detailed analysis of localized strength, enhancing its engineering reference value. This approach can potentially reduce hull weight while ensuring strength requirements and improving navigation performance and economic efficiency.

Future research should focus on leveraging hydrodynamic methods for full-period transient wave condition analysis to precisely identify the maximum stress and corresponding operational scenarios. This approach has the potential to refine planing hull structural designs, enhance the safety and efficiency of high-speed vessels, and contribute to advancements in marine engineering.

ACKNOWLEDGEMENTS

This research was funded by the National Key R&D Program of China, grant number 2021YFC2803400.

REFERENCES

[1] Kim, M. S., Jung, K. H., Park, S. B., 2018. Wave induced coupled motions and structural loads between two offshore floating structures in waves. *Brodogradnja*, 69(3), 149-173. https://doi.org/10.21278/brod69309

[2] Duan, J., Pei, Z., Zhang, L., 2025. A CFD-FEA coupling method for collapse characteristics analysis on bulk carriers under waves after flooding. *Ocean Engineering*, 324, 120787. https://doi.org/10.1016/j.oceaneng.2025.120787

[3] China Classification Society., 2023. Rules for Classification of Sea-Going Steel Ships. *China Communications Press*.

[4] Rosén, A., Garme, K., Razola, M., Begovic, E., 2020. Numerical modelling of structure responses for high-speed planing craft in waves. *Ocean Engineering*, 217, 107897. https://doi.org/10.1016/j.oceaneng.2020.107897

[5] Aman, Z., Xiongliang, Y., Mingliang, H., Wenhe, L., 2006. Research on the Loading Mode of Surface Ship under Wave Load Condition. *Chinese Journal of Ship Research*, 1(5-6), 9-14.

[6] Seo, D., Jeong, K. L., 2019. Numerical study on the prediction of the bow flare slamming pressure for the container ship in regular wave. *Brodogradnja*, 70(1), 25-42. https://doi.org/10.21278/brod70103

[7] Judge, C., Mousaviraad, M., Stern, F., Lee, E., Fullerton, A., Geiser, J., Schleicher, C., Merrill, C., Weil, C., Morin, J., Jiang, M., Ikeda, C., 2020. Experiments and CFD of a high-speed deep-V planing hull-Part I: Calm water. *Applied Ocean Research*, 96, 102060. https://doi.org/10.1016/j.apor.2020.102060

[8] Judge, C., Mousaviraad, M., Stern, F., Lee, E., Fullerton, A., Geiser, J., Schleicher, C., Merrill, C., Weil, C., Morin, J., Jiang, M., Ikeda, C., 2020. Experiments and CFD of a high-speed deep-V planing hull-part II: Slamming in waves. *Applied Ocean Research*, 97, 102059. https://doi.org/10.1016/j.apor.2020.102059

[9] Liu, W., Qin, Y., Hu, Y., Vladimir, N., Xu, S., Wu, Y., 2025. Numerical research on impacting load and structural response for a model experiment of high-speed craft. *Journal of offshore mechanics and Arctic engineering*, 147(1). https://doi.org/10.1115/1.4065153

[10] Abd Samad, F. I. B., Mohd Yusop, M. Y., Shaharuddin, N. M. R., Ismail, N., Yaakob, O. B., 2021. Slamming Impact Accelerations Analysis On Small High Speed Passenger Crafts. *Brodogradnja*, 72(1), 79-94. https://doi.org/10.21278/brod72104

[11] Volpi, S., Diez, M., Sadat-Hosseini, H., Kim, D. H., Stern, F., Thodal, R. S., Grenestedt, J. L., 2017. Composite bottom panel slamming of a fast planing hull via tightly coupled fluid-structure interaction simulations and sea trials. *Ocean engineering*, 143, 240-258. https://doi.org/10.1016/j.oceaneng.2017.07.053

[12] Diez, M., Lee, E. J., Harrison, E. L., Powers, A. M. R., Snyder, L. A., Jiang, M. J., Bay, R. J., Lewis, R. R., Kubina, E. R., Mucha, P., Stern, F., 2022. Experimental and computational fluid-structure interaction analysis and optimization of deep-V planing-hull grillage panels subject to slamming loads-Part I: Regular waves. *Marine Structures*, 85, 103256. https://doi.org/10.1016/j.marstruc.2022.103256

[13] Lee, E. J., Diez, M., Harrison, E. L., Jiang, M. J., Snyder, L. A., Powers, A. M. R., Bay, R. J., Serani, A., Nadal, M. L., Kubina, E. R., Stern, F., 2024. Experimental and computational fluid-structure interaction analysis and optimization of Deep-V planing-hull grillage panels subject to slamming loads-Part II: Irregular waves. *Ocean engineering*, 292, 116346. https://doi.org/10.1016/j.oceaneng.2023.116346

[14] Begovic, E., Bertorello, C., Bove, A., Garme, K., Lei, X., Persson, J., Petrone, G., Razola, M., Rosén, A., 2020. Experimental modelling of local structure responses for high-speed planing craft in waves. *Ocean Engineering*, 216, 107986. https://doi.org/10.1016/j.oceaneng.2020.107986

[15] Takami, T., Oka, M., Iijima, K., 2017. Study on application of CFD and FEM coupling method to evaluate dynamic response of ship under severe wave condition. *International Conference on Offshore Mechanics and Arctic Engineering*. American Society of Mechanical Engineers, 57731: V07AT06A053. https://doi.org/10.1115/OMAE2017-61553

[16] Takami, T., Matsui, S., Oka, M., Iijima, K., 2018. A numerical simulation method for predicting global and local hydroelastic response of a ship based on CFD and FEA coupling. *Marine Structures*, 59, 368-386. https://doi.org/10.1016/j.marstruc.2018.02.009

[17] Takami, T., Iijima, K., 2020. Numerical investigation into combined global and local hydroelastic response in a large container ship based on two-way coupled CFD and FEA. *Journal of Marine Science and Technology*, 25, 346-362. https://doi.org/10.1007/s00773-019-00668-7

[18] Xiao, J., Liu, C., Han, B., Wan, D., Wang, J., 2024. A two-way coupled fluid-structure interaction method for predicting the slamming loads and structural responses on a stiffened wedge. *Physics of Fluids*, 36(7). https://doi.org/10.1063/5.0212806

[19] Lu, T., Wang, J., Liu, K., Zhao, X., 2024. Experimental and numerical prediction of slamming impact loads considering fluid-structure interactions. *Journal of Marine Science and Engineering*, 12(5), 733. https://doi.org/10.3390/jmse12050733

[20] Alexandru, I., Brizzolara, S., Viviani, M., Couty, N., Donner, R., Hermundstad, O., Kukkanen, T., Malenica, S. and Temarel, P., 2007. Comparison of experimental and numerical impact loads on ship-like sections. *Advancements in Marine Structures: Proceedings of Marstruct 2007, the 1st International Conference on Marine Structures*. Taylor & Francis, 339-349.

[21] Paik, K. J., Carrica, P. M., Lee, D., Maki, K., 2009. Strongly coupled fluid-structure interaction method for structural loads on surface ships. *Ocean Engineering*, 36(17-18), 1346-1357. https://doi.org/10.1016/j.oceaneng.2009.08.018

[22] Maki, K. J., Lee, D., Piro, D. J., Collette, M., 2010. Hydroelastic Impact of Stern Structure Using CFD and FEA. *Proceedings of the 2010 Conference on Grand Challenges in Modeling & Simulation* (pp. 231-238).

[23] Jiao, J., Huang, S., Soares, C. G., 2021. Viscous fluid-flexible structure interaction analysis on ship springing and whipping responses in regular waves. *Journal of Fluids and Structures*, 106, 103354. https://doi.org/10.1016/j.jfluidstructs.2021.103354

[24] Chen, Z., Jiao, J., Wang, Q., Wang, S., 2022. CFD-FEM simulation of slamming loads on wedge structure with stiffeners considering hydroelasticity effects. *Journal of Marine Science and Engineering*, 10(11), 1591. https://doi.org/10.3390/jmse10111591

[25] Jiao, J., Chen, Z., Xu, S., 2024. CFD-FEM simulation of water entry of aluminium flat stiffened plate structure considering the effects of hydroelasticity. *Brodogradnja*, 75(1), 75108. https://doi.org/10.21278/brod75108

[26] Liang, L., Baoji, Z., Hao, Z., Hailin, T., Weijie, W., 2023. Hydrodynamic performance optimization of marine propellers based on fluid-structure coupling. *Brodogradnja*, 74(3), 74308. https://doi.org/10.21278/brod74308

[27] Liu, W., Zhang, Y., Xia, T., Lu, Y., Yang, M., Wu, W., Song, X., 2023. Numerical simulation of structural collapse of container ship in waves based on two-way coupled CFD and nonlinear FEA. *Chinese Journal of Ship Research*, 18(6), 49.

[28] Löhner, R., Cebral, J. R., Yang, C., Baum, J. D., Mestreau, E. L., Soto, O., 2006. Extending the range and applicability of the loose coupling approach for FSI simulations. *Fluid-Structure Interaction: Modelling, Simulation, Optimisation* (pp. 82-100). Springer Berlin Heidelberg. https://doi.org/10.1007/3-540-34596-5_4

[29] Li, H., Han, B., Liu, S., Chen, S., Wang, Z., Deng, B., 2024. A review of the numerical strategies for solving ship hydroelasticity based on CFD-FEM technology. *Ships and Offshore Structures*, 19(11), 1912-1930. https://doi.org/10.1080/17445302.2024.2317040

[30] China Classification Society, 2022. Rules for Construction and Classification of Sea-Going High Speed Craft. *China Communications Press*.